

THE PROTON RADIOGRAPHY CONCEPT

H.-J. Ziock, K. J. Adams, K. R. Alrick, J. F. Amann, J. G. Boissevain, M. L. Crow, S. B. Cushing, J. C. Eddleman, C. J. Espinoza, T. T. Fife, R. A. Gallegos, J. Gomez, T. J. Gorman, N. T. Gray, G. E. Hogan, V. H. Holmes, S. A. Jaramillo, N. S. P. King, J. N. Knudson, R. K. London, R. P. Lopez, J. B. McClelland, F. E. Merrill, K. B. Morley, C. L. Morris, C. T. Mottershead, K. L. Mueller, Jr., F. A. Neri, D. M. Numkena, P. D. Pazuchanics, C. Pillai, R. E. Prael, C. M. Riedel, J. S. Sarracino, H. L. Stacy, B. E. Takala, H. A. Thiessen, H. E. Tucker, P. L. Walstrom, G. J. Yates, J. D. Zumbro
(Los Alamos National Laboratory, Los Alamos, NM 87545)

E. Ables, M. B. Aufderheide, P. D. Barnes Jr., R. M. Bionta, D. H. Fujino, E. P. Hartouni, H.-S. Park, R. Soltz, D. M. Wright
(Lawrence Livermore National Laboratory, Livermore, CA 94550)

S. Balzer, P. A. Flores, R. T. Thompson
(Bechtel, Nevada, Los Alamos Operations, Los Alamos, NM 87545)

R. Prigl, J. Scaduto, E. T. Schwaner
(Brookhaven National Laboratory, Upton, NY 11973)

A. Saunders
(University of Colorado, Boulder, CO 80309)

J. M. O'Donnell
(University of Minnesota, Minneapolis, MN 55455; current address: Los Alamos National Lab)

ABSTRACT

Proton radiography is a new tool for advanced hydrotesting. It is ideally suited for providing multiple detailed radiographs in rapid succession (~ 200 ns between frames), and for work on thick systems (100's of g/cm² thick) due to the long nuclear interaction lengths of protons. Since protons interact both via the Coulomb and nuclear forces, protons can simultaneously measure material amounts and provide material identification. By placing cuts on the scattering angle using a magnetic lens system, image contrast can be enhanced to give optimal images for thick or thin objects. Finally the design of a possible proton radiography facility is discussed.

INTRODUCTION

We have developed a versatile new technique for obtaining a large number of flash radiographs in rapid succession. Our work is in support of the US Department of Energy's Science Based Stockpile Stewardship (SBSS) program and, in particular, is aimed at developing a concept for the Advanced Hydrotest Facility (AHF). The cessation of all underground nuclear weapons tests by the United States in accord with a proposed Comprehensive Test Ban Treaty has presented a significant challenge for the Department of Energy (DOE) nuclear weapons program with respect to certifying the performance, reliability, and safety of US nuclear weapons. The AHF is to be the ultimate above ground experimental tool for addressing physics questions relating to the safety and performance of nuclear weapon primaries.¹ In particular, the goal of the AHF is to follow the hydrodynamic evolution of dense, thick objects driven by high explosives.

The radiographic technique we developed uses high energy protons as the probing particles. The technique depends on the use of magnetic lenses to compensate for the small angle multiple Coulomb scattering (MCS) that occurs as the charged protons pass through the object under study. The use of a magnetic lens turns the otherwise troubling complications of MCS into an asset. Protons undergo the combined processes of nuclear scattering, small angle Coulomb scattering, and energy loss, each with its own unique dependence on material properties {atomic weight, atomic number (*Z*), electron configuration, and density}. These effects make possible the simultaneous determination of both material amounts and material identification. This multi-phase interaction suite also provides the flexibility to tune the sensitivity of the technique to make it useful for a wide range of material thicknesses.

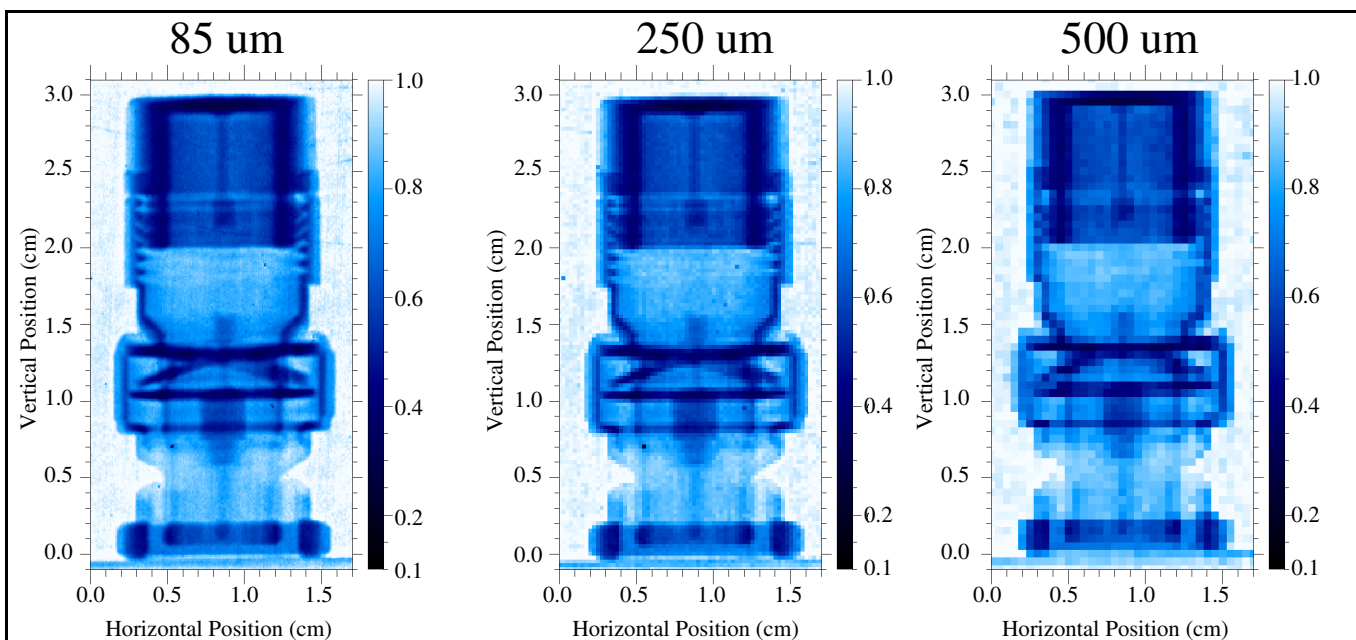


Fig. 1. A digitized phosphor image plate³ proton radiograph of a 50Ω BNC terminator. The initial image (left) was digitized with $(85 \mu\text{m})^2$ pixels. For the central and right images, pixels in 3-by-3 and 6-by-6 areas from the left image were summed.

The magnetic optics provides a means of maintaining unit magnification between the object and the image and the ability to move the image and hence detector planes far from the explosive object under test. This greatly improves the signal to background value and reduces the complexity of the blast protection scheme for the detectors. The magnetic lens system also provides the capability to change the angular acceptance, which is crucial for the ability to perform material identification and to tune the sensitivity for objects of very different thicknesses.

Protons offer a number of other advantages as probing particles in radiography as they can be detected with 100% efficiency and the same proton can be detected multiple times by multiple detector layers. For applications, such as those foreseen at the AHF, where thick dense dynamic objects need to be radiographed multiple times in very rapid succession, protons are nearly ideal solutions as they are highly penetrating, and the proton sources (accelerators) naturally provide the extended trains of short duration, high intensity beam bursts that are required. A single accelerator can easily provide enough intensity to allow the beam to be split many times to provide the multiple beams needed for simultaneous views of the object allowing 3-D tomographic “movies” to be made, the ultimate goal of the AHF.

The following sections of this paper will present an overview of the principles of high energy proton radiography (PRAD), their implementation, and how these mesh with the currently perceived performance requirements for the AHF. In addition, some of our initial PRAD results using both the 800 MeV beam available at the Los Alamos Neutron Scattering Center (LANSCE) and a secondary 10 GeV proton beam at the Alternating Gradient Synchrotron (AGS) at the Brookhaven National Laboratory (BNL) will be given. Finally, a possible design for an AHF is examined. In a separate paper² in these proceedings, we discuss the detector development effort associated with our work on PRAD.

GOALS

Performance requirements for the AHF are given in Table 1. In addition to the high frame rate requirements, high resolution images are needed. A feeling for resolution can be gathered from Fig. 1, in which pixels from a proton radiograph image have been averaged to ever coarser bins. The high resolution, high contrast capabilities must be achieved even for radiographs of “thick”

| Table 1: Desired AHF Performance Parameters | |
|---|---------------------------------------|
| Spatial Resolution | better than 1 mm (FWHM) |
| Object thickness | up to 100's of g/cm^2 |
| Thickness accuracy | ~ 1% pixel by pixel |
| Interframe spacing | from ~ 100 ns to many μs |
| # of frames | at least 10 |
| Velocities to freeze | speeds of km/s |
| Views for 3D imaging | 4 to 16 |

objects, where “thick objects” are measured in units of 100’s of g/cm². Thick objects strongly attenuate the beam of probing particles in their region of maximum thickness, and potentially produce large amounts of background by scattering particles from thinner regions of the object into the area of the image corresponding to the thickest part of the object where few direct particles penetrate. Background issues are further complicated by the need to view the object simultaneously from several directions, leading to the potential for scattering particles from one source into the detectors corresponding to another source. Tied to the requirement for high precision measurements is the desire to obtain maximum precision with a limited budget of probing particles. This is further constrained by the dynamic range of the detector system, which must count the number of transmitted particles in both the thin and thick regions of the object. In the following section, the properties of the ideal probing particle will be derived, and we will show that protons come very close to being such particles.

DESIRED PARTICLE ATTENUATION LENGTH

With a fixed budget of incident particles, one can calculate the ideal attenuation length (λ) for the probing particles when radiographing an object of a given thickness (L). The ideal attenuation length will be the one that minimizes the fractional error in the difference between the number of particles transmitted by two regions of the object that differ in thickness by an amount T . We start by assuming simple exponential attenuation of the beam by the object

$$N(L) = N_o \exp(-L/\lambda), \quad (1)$$

where N_o is the number of incident particles per pixel, which is assumed to be known. The difference in the number of particles transmitted through the two regions is given by

$$N(L) - N(L+T) = N_o \exp(-L/\lambda) - N_o \exp(-(L+T)/\lambda) = N_o \exp(-L/\lambda) [1 - \exp(-T/\lambda)]. \quad (2)$$

The error in the result given by eq. (2) is simply the square root of the sum of the squares of the errors in each of the terms in the difference. Since, from counting statistics, the square of the error in $N(L)$ is simply $N(L)$, we have

$$\text{error in difference} = [N(L) + N(L+T)]^{1/2} = [N_o \exp(-L/\lambda)]^{1/2} [1 + \exp(-T/\lambda)]^{1/2}. \quad (3)$$

In the limit of $T \rightarrow 0$, $\exp(-T/\lambda) \rightarrow 1 - T/\lambda$, and eqs. (2) and (3) become respectively

$$N(L) - N(L+T) = N_o \exp(-L/\lambda) [T/\lambda] \quad (4)$$

$$\text{error in difference} = [N(L) + N(L+T)]^{1/2} = [N_o \exp(-L/\lambda)]^{1/2} [2]^{1/2}. \quad (5)$$

Taking the ratio of eq. (5) to eq. (4) in order to get the fractional error gives

$$\text{fractional error in difference} = [2N_o \exp(-L/\lambda)]^{1/2} / \{N_o \exp(-L/\lambda) [T/\lambda]\} = 2^{1/2} T^{-1} \lambda N_o^{-1/2} \exp(L/2\lambda). \quad (6)$$

Taking the derivative of that with respect to λ and setting the result to zero in order to find the value of λ that minimizes the fractional error gives

$$(d/d\lambda) [\text{fractional error in difference}] = (2N_o)^{-1/2} T^{-1} \exp(L/2\lambda) [1 - L/2\lambda] = 0. \quad (7)$$

Solving for λ , we find

$$\lambda = L/2, \quad (8)$$

namely the optimal attenuation length is one half the object thickness. Thus for thick objects measured in units of 100’s of g/cm², one wants attenuation lengths measured in the same units, not in 10’s of g/cm². Table 2 gives nuclear interaction lengths for high energy protons (above kinetic energies of ~800 MeV nuclear interaction length values are largely energy independent) and attenuation lengths for 5 MeV x-rays (which have approximately the maximum penetrating depths in high Z materials). Also presented are the resulting *fractional error in difference* values as calculated using eq. (6) and assuming $N_o = 100,000$ and $T = 0.01 * L$ (i.e. a 1% thickness difference effect). Since this fractional error must be less than one for there to be any chance of seeing the thickness difference, the table clearly demonstrates the advantage of protons for thick, high Z objects.

MULTIPLE COULOMB SCATTERING

Unlike x-rays, protons undergo a random walk as they pass through an object due to the myriad of small angle charged particle collisions they have with the atoms in the object. This multiple Coulomb scattering (MCS), at first glance appears to be a great disadvantage for proton radiography since the protons no

Table 2: Nuclear interaction lengths for protons and x-ray attenuation lengths⁴ and the *fractional error in difference* values for a 1% thickness difference and 100,000 incident particles per pixel.

| | High Energy Protons ($\sim \geq 1$ GeV) | | | | 5 MeV x-rays | | | |
|--------------------------------|--|----------|-------|-------|--------------|----------|-------|---------|
| material | hydrogen | graphite | iron | lead | hydrogen | graphite | iron | lead |
| λ (g/cm ²) | 50.8 | 86.3 | 131.9 | 194.0 | 21 | 38 | 34 | 23 |
| X_o (g/cm ²) | 63.05 | 42.70 | 13.84 | 6.37 | | | | |
| L (g/cm ²) | | | | | | | | |
| 10 | 2.51 | 4.09 | 6.13 | 8.90 | 1.19 | 1.94 | 1.76 | 1.28 |
| 20 | 1.38 | 2.17 | 3.18 | 4.57 | 0.76 | 1.11 | 1.02 | 0.79 |
| 50 | 0.74 | 1.03 | 1.43 | 1.97 | 0.62 | 0.66 | 0.63 | 0.61 |
| 100 | 0.61 | 0.69 | 0.86 | 1.12 | 1.02 | 0.63 | 0.66 | 0.90 |
| 200 | 0.81 | 0.61 | 0.63 | 0.73 | 5.49 | 1.18 | 1.44 | 3.98 |
| 500 | 6.23 | 1.40 | 0.79 | 0.63 | 2779.31 | 24.46 | 47.46 | 1081.10 |

longer travel in a straight line, and an image, unless taken immediately downstream of the object, will be blurred because of the angular dispersion. (Even immediately downstream of the object, some blurring due to the random walk will be evident.) To first order, the plane projected MCS angular distribution of the protons leaving the object is a Gaussian characterized by a root mean square (*rms*) plane projection deflection angle θ_o which is given by the expression⁴

$$\theta_o(z) = 0.0136 \text{ GeV } (\beta c p)^{-1} (z/X_o)^{1/2} [1 + 0.038 \ln(z/X_o)] \quad (9)$$

where c is the velocity of light, βc is the velocity of the proton, p is its momentum, and z/X_o is the thickness of the object, z , measured in units of radiation length, X_o . It should be noted that as the β of the proton approaches one, θ_o depends inversely on the momentum of the proton, and only grows as the square root of the object thickness. (The logarithmic term is on the order of 10% and has been ignored here.) The MCS has two effects. The first is the random walk itself, which leads to the limited blurring previously mentioned and is characterized by plane projection *rms* deviation, y , of the proton from its unscattered location by the time it reaches the end of the object. That is given by

$$y(z) = 3^{-1/2} z \theta_o(z). \quad (10)$$

The second is the additional blurring due to the random direction of the protons from MCS as they leave the object and travel to the detector, which will be located a non-zero distance from the object. The first effect can be dealt with by simply raising the proton beam momentum. To set the scale, for proton beams of 2, 5, 20, and 50 GeV/c beam, for a 20 radiation length object which is 10 cm thick, $y = 2.16, 0.80, 0.20,$ and 0.08 mm respectively. As seen from eqs. (9) and (10), the results improves linearly as the beam momentum is increased, but grow worse as the product of the linear thickness of the object and the square root of the thickness of the object in radiation lengths. Since the object one wants to radiograph has a known thickness, by choosing a sufficiently high momentum, the blur can be reduced to any desired value. The *rms* angles θ_o for the same geometry and beam momenta are 37.4, 13.8, 3.4, and 1.4 milliradians respectively. Since we intend to look at explosively driven dynamic objects, the detectors need to be quite distant from the object. Thus the second effect must be dealt with by a different means. The solution here relies on the fact that protons are charged and therefore their trajectories can be bent by a magnetic field. More specifically, one builds a magnetic lens. The center of the object is then placed at the object plane of the long focal length magnetic lens. Similar to an optical lens, the magnetic lens collects all the protons within its solid angle acceptance, and, regardless of their angle of emission from a point in the object plane, puts them all back at the corresponding point in the image plane.

MAGNETIC LENS AND MATERIAL IDENTIFICATION

The overall magnetic lens system we have designed⁵ is shown schematically in Fig. 2. The two imaging lens cells thereof are inverting identity ($-I$) lenses. These cells are each comprised of four identical quadrupole magnets operated at identical field strengths, but alternating polarities ($+ - + -$). They have the feature that at the center of the gap between the two middle magnets of a cell, the protons are sorted radially solely by their scattering angle in the object, regardless of which point in the object plane they originated from. This allows one to place a collimator at that location and use it to make cuts on the MCS

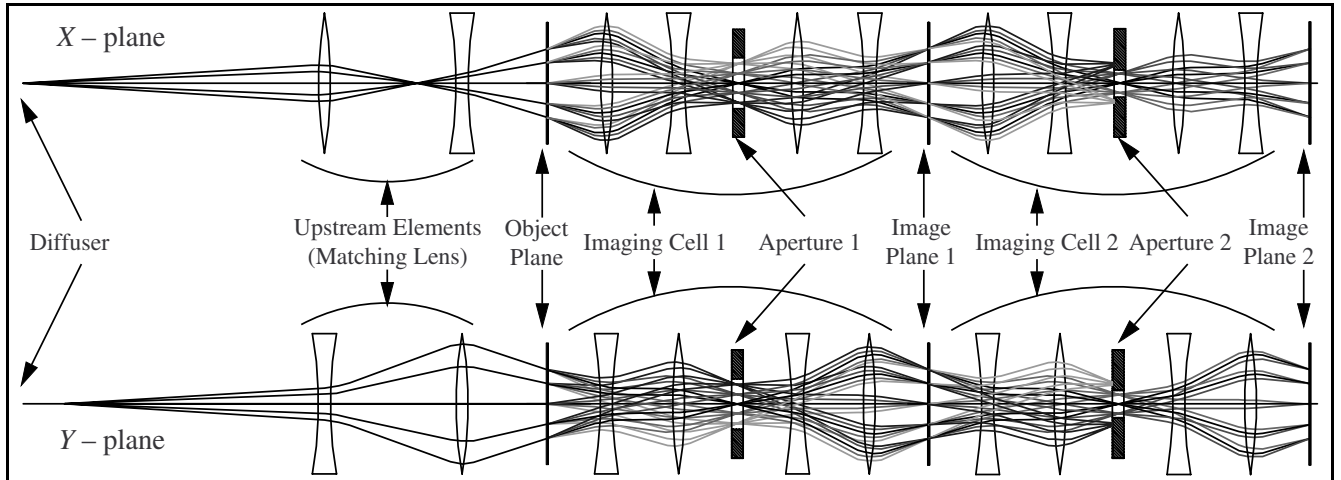


Fig. 2 Schematic of the PRAD magnetic lens system showing both the X and Y views. The beam is first prepared with a diffuser and matching lens to meet optics requirements. It then passes through the object being radiographed. The transmitted beam passes through an iris, or aperture located in the middle of the 4-quadrupole $-I$ magnetic lens cell and is focused on the first detector. It then enters the second identical $-I$ lens cell, which this time has a smaller diameter iris, and is focused on a second detector. Together, the two detectors provide the information needed to reconstruct both the density profile and material composition of the object.

angle in the object. As noted previously, the scattering angle distribution is approximately a Gaussian with a width, which, by eq. (9), depends on the number of radiation lengths of material the protons passed through. With the collimator, one can limit the transmitted particles to only those with an MCS angle less than the cut angle (θ_c). The number of transmitted particles N_c after such a cut is given by

$$N_c \approx N \int_0^{\theta_c} \frac{1}{2\pi\theta_o} \exp\left(-\frac{\theta^2}{2\theta_o^2}\right) d\Omega \approx N \left[1 - \exp\left(-\frac{\theta_c^2}{2\theta_o^2}\right) \right], \text{ or } \frac{N_c}{N} \approx \left[1 - \exp\left(-\frac{\theta_c^2}{2\theta_o^2}\right) \right] \quad (11)$$

where N is the number of incident particles. Note that when $\theta_c \gg \theta_o$, $N_c = N$, as expected. Using eq. (9) for θ_o , ignoring the small logarithmic term, and solving for z/X_o gives

$$\frac{z}{X_o} \approx \frac{-\theta_c^2}{2\left(\frac{13.6 \text{ MeV}}{\beta cp}\right)^2 \ln\left(1 - \frac{N_c}{N}\right)} \quad (12)$$

If we now build a lens system which consists of two of the $-I$ lenses set back to back, the first with an aperture sufficient to pass essentially all the particles scattered by MCS (but not those scattered by inelastic nuclear interactions), the second with its aperture set so that it cuts into the MCS distribution, and then place detectors at the image planes of the two lenses, we get two independent measurements. The first depends on the number of nuclear interaction lengths of material in the object, while the second depends on the number of radiation lengths of material in the object. Since the values of nuclear interaction length and radiation length have different dependencies on material type as shown in Table 2, we are in a position to determine both the amount of material in the object and what that material is. If the object has transitions from one material type to two material types and then from two to three material types, ..., we can unfold the object in terms of material types and thickness for each material. (Note that a 1 to 2 material step followed by a 2 to 3 material step can be unfolded, but a sudden 1 to 3 material step cannot be unfolded.)

It should also be noted that by using a single magnetic lens with just a MCS angle cut, one can achieve high contrast proton radiography even when the object is too thin to provide good contrast using nuclear attenuation. Just as was the case for nuclear exponential beam attenuation, for pure MCS based radiography of a given thickness object, there is an ideal cut angle that maximizes sensitivity to changes in object thickness. The value of that optimal cut angle can be determined by the same process as lead to eq. (8), but for an attenuation that is given by eq. (11). Thus by changing the aperture to provide that optimal

MCS angle cut, one can tune the system to provide optimum sensitivity, regardless of the object thickness. This was done for the image shown in Fig. 1.

As can be seen in Fig. 2, the magnetic lens system has some additional elements upstream of the object. The proton beam passes through a thin diffuser, which gives a small angular divergence to the beam and then passes through a set of magnets, which introduces a correlation between the radial position of a proton in the object plane and its angle. This is done to reduce magnetic lens induced aberrations in the identity lens cells. These aberrations are both geometric and chromatic in nature. For the particular momentum to which the lens is tuned, the relation between the location of a particle in the object plane, x_{object} , and its location in the image plane, x_{image} , for a magnetic lens is given by

$$x_{image} = R_{11}x_{object} + R_{12}\phi_x, \quad (13)$$

where ϕ_x is the angle of the particle in the x -plane relative to the axis of the lens, and the R 's are constants, which characterize the magnetic lens. A similar equation holds for the y -coordinate. If instead of having beam particles with a single momentum (p), the particles have a spread in momentum, δp , eq. (13) becomes

$$x_{image} = (R_{11} + \Delta R_{11}' + \text{higher order terms})x_{object} + (R_{12} + R_{12}'\Delta + \text{higher order terms})\phi_x, \quad (14)$$

where $\Delta \equiv \delta p/p$ and the R' coefficients are distortion constants for the lens. When an object is placed in the object plane, several things happen to the transmitted proton beam. First, the protons lose energy and thus momentum; their final average momentum p , being less than their incident momentum p_o . The momentum loss in the object is not single valued, but instead covers a range $\pm \delta p$ due to random nature of the energy loss process and variations in the thickness of the object. Also, through MCS, an angular divergence is introduced to the beam, which is characterized by θ_o , as given by eq. (9).

We are free to arrange the incident proton beam so that all the particles incident on the object plane have a relation between their angle and location in that plane given by $\phi_x = wx$. Combining this with the effect of the MCS, we have $\phi_x = wx + \theta_o$ for the outgoing beam. Assuming the magnetic lens is tuned to the average momentum of the transmitted protons, eq. (14) becomes

$$x_{image} = R_{11}x_{object} + R_{12}\phi_x + (R_{11}' + wR_{12}')x_{object}\Delta + R_{12}'\theta_o\Delta + \text{higher order terms}. \quad (15)$$

Making use of the fact that we have a $-I$ lens, which implies $R_{11} = -1$ and $R_{12} = 0$, and ignoring the *higher order terms*, eq. (15) becomes

$$x_{image} = -x_{object} + (R_{11}' + wR_{12}')x_{object}\Delta + R_{12}'\theta_o\Delta. \quad (16)$$

We note that if we choose w such that $w = -R_{11}'/R_{12}'$, the $x_{object}\Delta$ term in eq. (16) becomes identically equal to zero, and thus all position dependent chromatic aberration terms vanish. The matching magnets upstream of the object are used to establish that correlation, w , between x and ϕ_x . Thus eq. (16) becomes

$$x_{image} = -x_{object} + R_{12}'\theta_o\Delta, \quad \text{provided:} \quad w = -R_{11}'/R_{12}'. \quad (17)$$

In addition to the matching lens establishing the desired correlation between incident particle angle and location at the object plane, the lens provides some other useful functions. It further expands the incident beam allowing one to illuminate a large object, without making the upstream diffuser very thick. It also helps maintain a very uniform acceptance across the full field of view of the imaging lenses.

MOMENTUM SCALING

The remaining distortion term in eq. (17) is given by

$$\Delta x = x_{object} + x_{image} = R_{12}'\theta_o\Delta, \quad (18)$$

which is characterized by the chromatic aberration coefficient of the lens, R_{12}' , and the product $\theta_o\Delta$. For high momentum protons (> 1 GeV/c), the momentum loss is essentially independent of beam momentum. Therefore the fractional momentum bite of the beam, Δ , scales inversely proportional to the beam momentum. Likewise from eq. (9), the angle θ_o is also inversely proportional to the beam momentum. Thus the spatial resolution of the magnetic lens system improves as the square of the beam momentum.

Other factors also effect the overall spatial resolution that can be attained in proton radiography. There is the spatial resolution of the detector system, which is essentially independent of momentum. There is also the effect of the non-zero thickness of the object, which by eq. (10) degrades the resolution. As discussed earlier, this effect scales as $1/p$. If there is a vessel to contain the explosive blast in an AHF application,

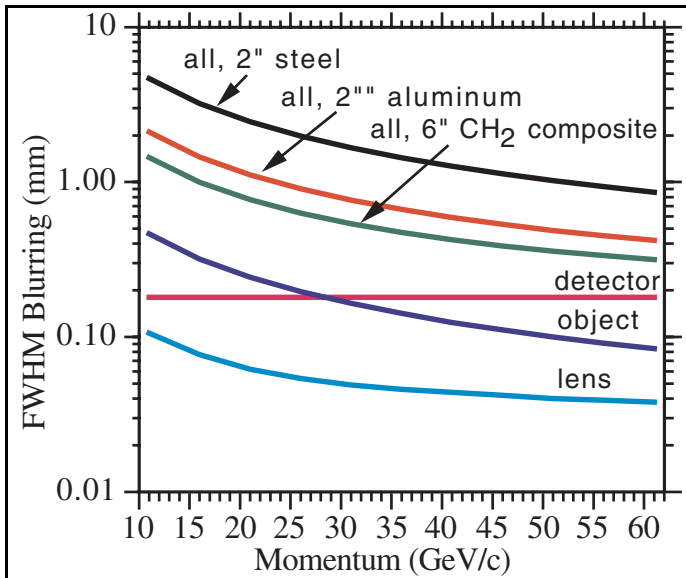


Fig. 3. The momentum scaling for the various terms effecting spatial resolution. Shown are possible individual contributions from the detector, object, and lens, and the overall contribution when these are combined with different containment vessels values.

chromatic spatial aberrations from the lens, which were already a higher order effect. In Fig. 3 we plot the expected overall spatial image blurring as a function of beam momentum for the various terms and various containment vessel walls.

PROTON DETECTION

Protons, being charged particles, directly excite the detector medium, predominantly through Coulomb interactions with electrons in the medium. They thus generate a signal even for an extremely thin detector. Because of the mass difference between protons and electrons, there is very little deflection of the protons by the detector, and therefore very little in the way of a detector produced background problem. In contrast, x-rays, being uncharged, do not directly ionize the detector material as they pass through it. As a matter of fact, it takes one x-ray attenuation length for 63% of the x-rays to interact and generate a charged particle, which then leaves the excitation trail that a detector sees. X-rays predominantly interact through large angle scattering, and due to the large required detector thickness are likely to have secondary interactions that produce backgrounds in the detector. Since protons can be detected by very thin detectors, no similar problem exists for them. Also in a thin detector, the proton is virtually undeflected and therefore can be used for a second (or third) time, such as in a second magnetic lens system for MCS material identification. Furthermore, multiple planes of detectors can detect the same proton, thereby achieving redundancy. The thinness of the proton detectors also makes them essentially blind to neutral secondary particles generated in the object (neutrons and γ -rays), thereby reducing the potential for other background problems.

BACKGROUNDS

Backgrounds in the case of proton radiography are very small, as we have verified both in Monte Carlo studies and in experiments. This results from the relatively long values of interaction (attenuation) lengths for protons and the large standoff distance for the detectors from the object, which is due to the magnetic lens system. The magnetic lens also provides filtering of off-momentum background particles. At the same time, the thin detectors are essentially blind to neutral secondary particles, which would otherwise dominate the relatively small background. In neither proton nor x-ray radiography are the "attenuated" particles cleanly removed from the beam. Some fraction of the "attenuated beam" will undergo one or several hard interactions in the object and/or surrounding material and still hit the detector in a location that

the MCS of the incoming and outgoing beams in the vessel walls will produce a similar effect, but this time linearly dependent on the separation between the object and the containment vessel wall. Due to the relatively large value of this distance, this will likely be the dominant term effecting spatial resolution. The MCS in the vessel wall will change the value of the outgoing proton angle, which cannot be corrected for by the magnetic lens. This characteristic angle change multiplied by the distance from the object to the vessel wall will be the amount of blur introduced. (If the vessel wall is closer to the image plane than the object plane, the relevant distance is the vessel wall to image plane separation.) The characteristic angle involved is again given by eq. (9) and thus scales as $1/p$. As eq. (9) also shows, it depends on the thickness of the vessel wall in units of radiation length, and therefore it is important to use thin, low- Z materials. The vessel wall thickness is less important for the incident beam, since there it affects the desired correlation between the incident particle location at the object and the particle angle there. This correlation was to remove the

is uncorrelated to their ideal path through the object. Thus they contribute a background signal in the detector, which is indistinguishable from the real signal, thereby masking or greatly diminishing one's sensitivity to the small effects one is looking for in the object. This is clearly a signal to background issue. The signal depends on the ability to get a substantial number of particles directly through the thickest part of the object, and thus requires a very large number of incident particles for a thick object. The background level depends on a combination of factors, the most important of which are the variation in thickness across the object in terms of scattering or attenuation length, the probability of scattering in a given amount of material, and the number of incident particles.

The background will clearly be worst when the object is thick and there is a considerable variation in thickness across the object. At the thickest part of the object there will be very little signal as the beam is strongly attenuated. In the thinner parts of the object, scattering of the beam will occur with some of the scattered particles deflected into the detector region corresponding to the thickest part of the object and potentially causing a large fractional background there. Thus ideally one would like to tailor the beam intensity to be highest at the thickest part of the object, and to have the thickness of the object roughly comparable to the attenuation length of the material of which the object is made. This is exactly what one has in proton radiography. The upstream diffuser used to impart the small angular divergence to the incident beam produces an approximately Gaussian shaped beam profile which is peaked at the center of the beam where one can locate the thickest part of the object. The width of the Gaussian can also be adjusted by changing the diffuser thickness, depending on whether a more uniform or more peaked beam is desired. Furthermore, the interaction length of the protons is, or can be, well matched to the thickness of the object. In contrast, for x-rays, there is typically a poor match of attenuation length to object thickness, especially for thick objects. Also, since the x-ray source is essentially a point source, the beam intensity is nearly uniform across the object. In practice, for x-ray images, a graded collimator of varying thickness can be built that is matched to the object so the collimator – object combination present a uniform thickness to the x-ray beam. However, in the case of dynamic radiography, that becomes problematic at best. An added complication occurs when one has multiple beam lines and detectors needed to perform 3-D reconstructions of the object. Crosstalk between the different beam lines and detectors can then occur. Furthermore, additional beam is incident on the object due to the multiple beam lines. For protons the magnetic lens maintains the signal intensity between the object and the detector plane, while particles failing to pass the angular acceptance cut of the lens are either stopped internally in the lens, or fall off in intensity as the distance from the object to the detector squared. With the long length of the magnetic lens, there is virtually no background from other beam lines.

A numerical example of the background issue dramatically demonstrates the difference between protons and x-rays. We will use a very simplistic model that demonstrates the gross features of the issue. We take an object which has a maximum thickness L , and a minimum thickness of fL , where $f < 1$. The signal at the thickest part of the object is given by eq. (1)

$$\text{signal} \equiv S = N_o \exp(-L/\lambda). \quad (19)$$

For a calculation of the background we again start with eq. (1), and substitute the distance the proton has penetrated into the object (x) in place of L . We then calculate the differential of that in order to calculate, as a function of x , the number of protons which undergo a scattering in a length dx . Ignoring the leading minus sign, which indicates a loss of particles from the incident beam, this gives

$$dN(x) = N_o \lambda^{-1} dx \exp(-x/\lambda). \quad (20)$$

Next we calculate the number of those $dN(x)$ scattered particles that make it out of the object. We do this at the thinnest part of the object where the distance the particles still have to travel to get out of the object is $fL - x$. (We ignore the fact that the particles are now traveling at an angle to their original direction and therefore have a somewhat greater distance to travel.) This calculation is again done using eq. (1) and we find the number of *surviving scattered* $\equiv SS$ particles to be

$$SS = dN(x) \exp[-(fL-x)/\lambda] = N_o \lambda^{-1} dx \exp(-x/\lambda) \exp[-(fL-x)/\lambda] = \{N_o \lambda^{-1} \exp(-fL/\lambda)\} dx. \quad (21)$$

Integrating eq. (21) over the thickness of the object at its thinnest location (*i.e.* $x: 0 \rightarrow fL$) gives

$$\text{total } SS = N_o \lambda^{-1} fL \exp(-fL/\lambda). \quad (22)$$

To find the *background* we just need to multiply the *total surviving scattered* value by the detector fractional acceptance at the region of thickest part of the object for those scattered particles. We take this to

Table 3: Signal to background values assuming $H = 0.001$.

| material | λ_{nuclear} (g/cm ²) | $\lambda_{5 \text{ MeV x-ray}}$ (g/cm ²) | L (g/cm ²) | f | $(S/N_o)_{\text{nuclear}}$ | $(S/N_o)_{\text{x-ray}}$ | S/B_{nuclear} | $S/B_{\text{x-ray}}$ | R_{nuclear} | $R_{\text{x-ray}}$ |
|----------|--|---|-----------------------------|-----|----------------------------|--------------------------|------------------------|----------------------|----------------------|--------------------|
| iron | 131.9 | 34 | 304 | 0.2 | 0.1 | 1.32E-04 | 344 | 0.4 | 6.3 | 1269.2 |
| iron | 131.9 | 34 | 212 | 0.2 | 0.2 | 1.94E-03 | 857 | 5.4 | 3.6 | 147.7 |
| iron | 131.9 | 34 | 91 | 0.2 | 0.5 | 6.79E-02 | 4143 | 216.3 | 1.7 | 8.6 |
| iron | 131.9 | 34 | 304 | 0.5 | 0.1 | 1.32E-04 | 275 | 2.6 | 3.2 | 87.0 |
| iron | 131.9 | 34 | 212 | 0.5 | 0.2 | 1.94E-03 | 556 | 14.1 | 2.2 | 22.7 |
| iron | 131.9 | 34 | 91 | 0.5 | 0.5 | 6.79E-02 | 2040 | 193.9 | 1.4 | 3.8 |
| lead | 194.0 | 23 | 447 | 0.2 | 0.1 | 3.67E-09 | 344 | 4.60E-05 | 6.3 | 5595334.9 |
| lead | 194.0 | 23 | 312 | 0.2 | 0.2 | 1.27E-06 | 857 | 7.07E-03 | 3.6 | 52062.9 |
| lead | 194.0 | 23 | 135 | 0.2 | 0.5 | 2.89E-03 | 4143 | 8.0 | 1.7 | 107.5 |
| lead | 194.0 | 23 | 447 | 0.5 | 0.1 | 3.67E-09 | 275 | 6.24E-03 | 3.2 | 16496.5 |
| lead | 194.0 | 23 | 312 | 0.5 | 0.2 | 1.27E-06 | 556 | 1.66E-01 | 2.2 | 886.8 |
| lead | 194.0 | 23 | 135 | 0.5 | 0.5 | 2.89E-03 | 2040 | 18.4 | 1.4 | 18.6 |

be H . Thus we find the *signal to background* value $\equiv S/B$ is given by

$$S/B = N_o \exp(-L/\lambda) / [H N_o \lambda^{-1} f L \exp(-fL/\lambda)] = \lambda(HfL)^{-1} \exp[-(1-f)L/\lambda]. \quad (23)$$

In Table 3 are given some values of the S/B for different materials, values of L , and values of f , both for 5 MeV x-rays and high energy protons. Also given are the beam transmission probabilities (S/N_o) at the thickest part of the object. We take $H = 0.001$. It should be noted that due to the limited momentum transmission of the magnetic lens in proton radiography, the value of H for protons should be less than that for x-rays, improving the S/B value for protons relative to that for x-rays beyond the values shown.

A related issue addressed in Table 3 is the dynamic range required for the detector. If a uniform intensity beam is incident on the object, the ratio, R , of the signal intensity at the thinnest part of the object to that at the thickest part of the object (ignoring background) is given by

$$R = N_o \exp(-fL/\lambda) / [N_o \exp(-L/\lambda)] = \exp((1-f)L/\lambda). \quad (24)$$

As Table 3 shows, R can be quite large for x-rays, especially when λ is small compared to L . In looking at these values and considering the detector dynamic range and sensitivity, it is important to keep in mind that the detector must, in addition, be able to see on the order of a 1% change in object thickness at the thickest part of the object.

The preceding calculations do not deal with the production of secondary particles in the object due to nuclear interactions. We examined this issue in a Monte Carlo study which used the latest version of the LAHET⁶ code, which in turn uses FLUKA⁷ to simulate the nuclear scattering and particle secondary production. In the study, a zero diameter beam of 50 GeV protons was incident normal to a slabs of ²³⁸U of different thicknesses. At the downstream face of the slab we recorded all outgoing particles. For those particles, their particle type, location, and 3-momentum were recorded. Neutrons were tracked down to kinetic energies of 20 MeV. Due to the inability of LAHET to directly deal with γ -rays, and electrons and positrons, these were ignored. The predominant source of γ -rays will be π^0 decays, whose number will be about the same as those for π^+ or π^- , the dominant secondary charged particles. As the π^0 decays essentially instantaneously, into two γ -rays, by the above arguments, their number will initially be about equal to the number of secondary charged particles. However, the γ -rays will be strongly attenuated in the object, and the few surviving γ -rays will be spread over a large angular region and thus outside the angular acceptance of the magnetic lens system. Since they are also nearly invisible to the detectors, their omission should have a negligible effect on the results. Fig. 4 gives the angular distribution of all the particles making it out of the back of the slab sorted by particle type. Fig. 5 shows a similar plot, but for outgoing particle momentum. Both figures are for 500 g/cm² of uranium, a very thick object, where the background problem will be most severe. In Table 4, we record the signal and background values for cuts on the outgoing particle angle and momentum for different slab thicknesses. We consider signal particles to be protons which have angles inside the outgoing angle cut, and a momentum which is greater than the expected average momentum of protons exiting the slab minus 5%. As can be seen, secondary particles contribute very little, and the dominant secondary particles are neutral and thus essentially invisible to the detector.

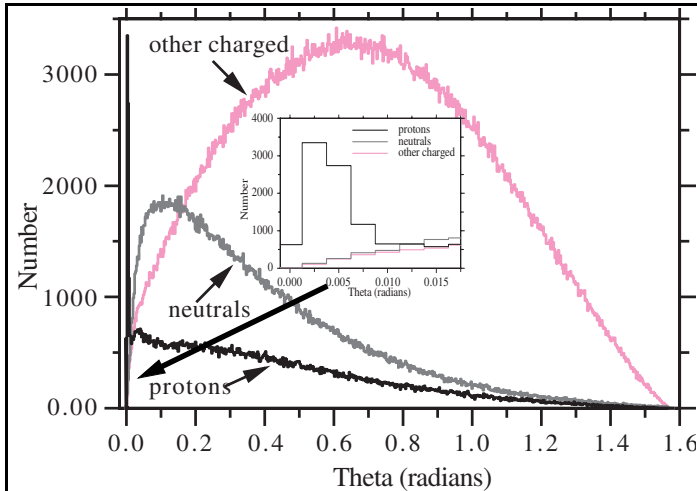


Fig. 4. Histograms of the number of outgoing particles of a particular type as a function of scattering angle for 100,000 incident 50 GeV protons on a 500 g/cm² slab of ²³⁸U.

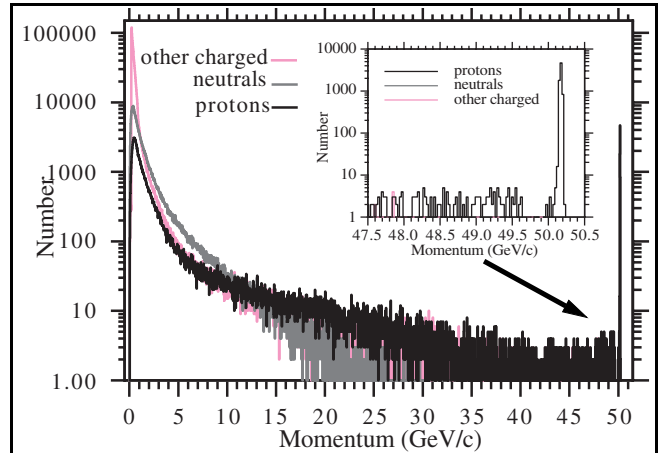


Fig. 5. Histograms of the number of outgoing particles of a particular type as a function of momentum for 100,000 incident 50 GeV protons on a 500 g/cm² slab of ²³⁸U.

EXPERIMENTAL WORK

We have carried out a number of experimental tests of the PRAD concept using magnetic imaging lenses. Some of these tests were carried out at the LANSCE facility, making use of its 800 MeV chopped proton beam. The 800 MeV beam energy is too low to allow for the study of thick objects in which nuclear attenuation is important. This is due to the large dispersion in momentum loss by the protons at 800 MeV, both directly and as a result of variations in object thickness. As discussed earlier, this results in poor lens performance and hence a blurred, poor quality image. However, by looking at thinner objects, we could still study the MCS part of the PRAD concept, the actual performance of the magnetic lens system, and by making use of the pulsed nature of the proton beam (one pulse every $N \times 358$ ns, $N = \text{integer}$), take a sequence of radiographs of explosively driven events.

The ability to take high contrast, high resolution images using a MCS angle cut for a thin object is demonstrated by the image shown in Fig. 1, which is a static radiograph taken using a phosphor image plate as a detector. The object is a 50 Ω BNC terminator that is only 1.4 cm in diameter. The resistor and its leads inside the metal case of the terminator are clearly visible, as are the internal screw threads. Even submillimeter features are sharp. Radiographic images of a dynamic event are shown in Fig. 6. The object is a 58 mm diameter half-sphere of high explosive (HE) which is in the process of detonating. These images were again made with phosphor image plates. Four different explosive shots were fired to produce the four radiographs, with the proton beam timed to arrive at different times relative to the detonation initiation time. The different times are (top to bottom) 0.99 μ s, 1.90 μ s, 2.50 μ s, and 3.25 μ s after detonation initiation. Also shown are the results of a reconstruction of the object from those radiographs. The position of the shock front (the glitch in Fig. 6) associated with the detonation is seen to progress between the different radiographs. The shock front is seen to correspond to about a 30% increase in local

| Table 4: Particle generation & survival in the given amount of ²³⁸ U | | | | |
|---|---------|-------------------------|----------------------------|------------------------------|
| | no cut | 10 mrad θ cut | 47.9 GeV/c momentum cut | momentum and θ cut |
| 50 g/cm² | | | | |
| protons | 151840 | 77756 | 77015 | 76761 |
| neutrals | 211620 | 633 | 21 | 11 |
| other charged | 196658 | 837 | 0 | 0 |
| 100 g/cm² | | | | |
| protons | 182034 | 60733 | 59584 | 59184 |
| neutrals | 448298 | 1017 | 36 | 14 |
| other charged | 331171 | 1364 | 0 | 0 |
| 200 g/cm² | | | | |
| protons | 212593 | 36998 | 35597 | 35134 |
| neutrals | 883247 | 1318 | 45 | 23 |
| other charged | 473650 | 1691 | 0 | 0 |
| 500 g/cm² | | | | |
| protons | 168694 | 8209 | 7473 | 7160 |
| neutrals | 1319912 | 935 | 11 | 5 |
| other charged | 397354 | 1044 | 0 | 0 |

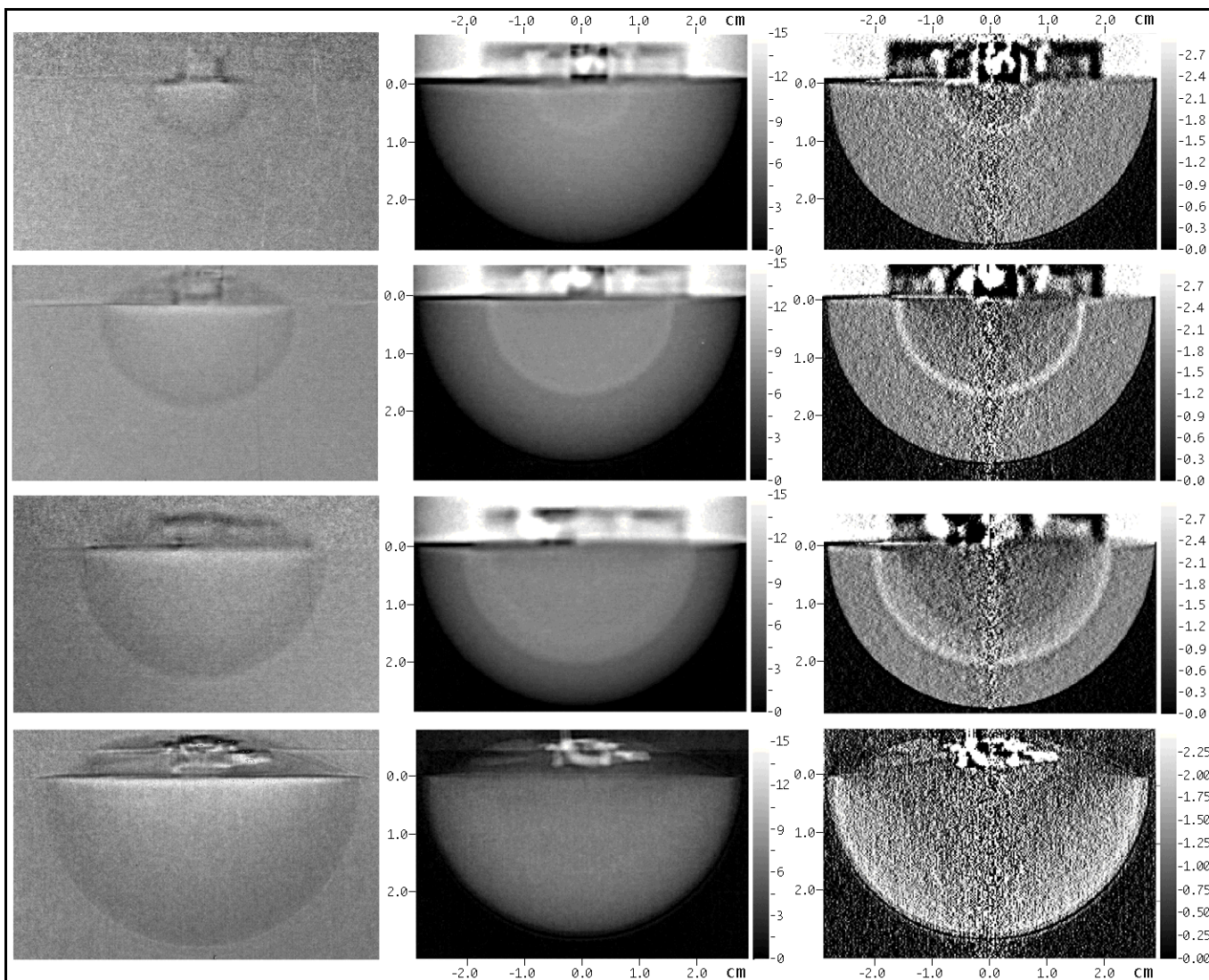


Fig. 6. Original data and reconstructions from phosphor image plate proton radiographs of a hemispherical piece of HE at different times following detonation (top to bottom: 0.99 μ s, 1.90 μ s, 2.50 μ s, and 3.25 μ s after detonation initiation). The left column is the ratio of a radiograph at the given time after detonation initiation to an identical radiograph taken prior to detonation. The central column gives the unfolded amount of material in units of g/cm^2 using the measured beam attenuation, the known radiation length for the HE material, and the known MCS angle cut. The right column is a reconstruction of the density of the material obtained using the preceding results and a hemispherical object shape. The reconstruction starts at the left and right edges of the object and works towards the vertical centerline of the object, resulting in the increased error seen towards the centerline.

density. Behind the shock front a rarefaction can also be seen. For the above images, the collimator inside the magnetic lens was set to provide a MCS angle cut of 10 milliradians.

To test the PRAD concept at higher energies, we made use of a 10 GeV secondary proton beam at the AGS at BNL. The various components of the experimental setup are shown in Fig. 7. As a secondary beam line was being used, the instantaneous proton beam flux was low, allowing us to use wire chambers to track the protons individually from upstream of the object location to the image plane of the magnetic lens. Images were made with both the wire chambers and phosphor image plates using long exposure times. One of the objects we imaged, also shown in Fig. 7, is known as the French Test Object (FTO) and consists of concentric spherical shells. The outer shell is a density 1/2 g/cc plastic foam and covers the radial region between 6.5 and 22.5 cm. The next inner shell is copper and is in the region between 4.5 and 6.5 cm. The third shell is a tungsten alloy and covers the region between 1 and 4.5 cm leaving an air

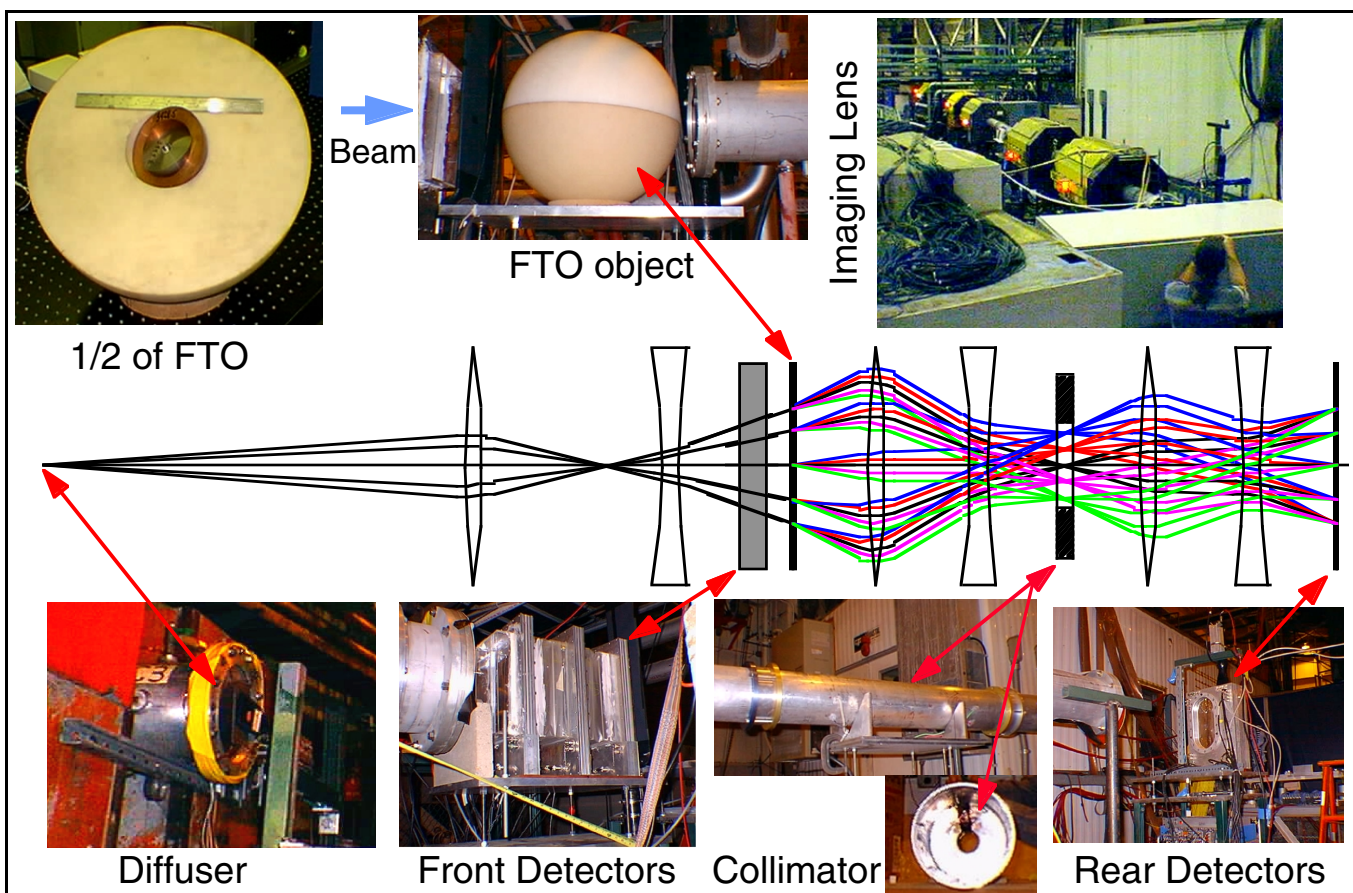


Fig. 7 Schematic of the PRAD magnetic lens system and actual components for EXP. 910 at the BNL AGS. The beam is first prepared with a diffuser and matching lens to meet optics requirements. Next the beam is measured just upstream of the object by the front detectors after which it passes through the object being radiographed. The transmitted beam passes through an iris, or aperture, located in the middle of the 4-quadrupole -I magnetic lens system and is focused on the rear detectors. The runs with different angle cuts were done separately using different collimators. The data from these runs provide the information needed to reconstruct both the density profile and material composition of the object.

cavity in the center. The maximum object thickness is 213 g/cm^2 , just tangent to the central cavity. The magnetic lens system had an effective horizontal and vertical aperture of about $\pm 7 \text{ cm}$. Two sets of images were taken of the FTO, one with a collimator corresponding to $\theta_c \sim 9 \text{ mrad}$, and the second with a collimator corresponding to $\theta_c \sim 4.5 \text{ mrad}$. The first collimator passes nearly all of the MCS distribution but not the nuclear inelastically scattered particles, whereas the second cuts substantially into the MCS distribution. The resulting image plate radiographs are shown in Fig. 8. Fig. 9 shows the radial distributions resulting from those radiographs and the “radiographs” of the beam intensity incident on the object. The results of a reconstruction of the object are shown in Fig. 10 and are given in Table 5, which also gives the actual locations of the changes in the material type and the Particle Data Book⁴ values for the nuclear interaction lengths and radiation lengths of the relevant materials. The results clearly demonstrate the ability to unfold material type and thickness.

We also used the wire chamber data to study background issues. The beam energy, although still a factor of about 5 less than that being discussed for the AHF, is sufficient to address most of the background problems, as one is well above the particle production threshold energies that will be most relevant at 50 GeV. The wire chambers consisted of multiple planes providing both X and Y information, which could in turn be used to provide particle direction information. As the magnetic lens used was a - I lens, summing the proton position at the object plane and the image plane should ideally give a value of zero regardless of the proton position in the object plane. This is shown in Fig. 11, where scatterplots of $YSUM = Y_{object} + Y_{image}$ versus $XSUM = X_{object} + X_{image}$ are given. Also shown are scatterplots of the particle scattering angle vs. $XSUM$. The upper left plot has a linear intensity scale showing that the vast

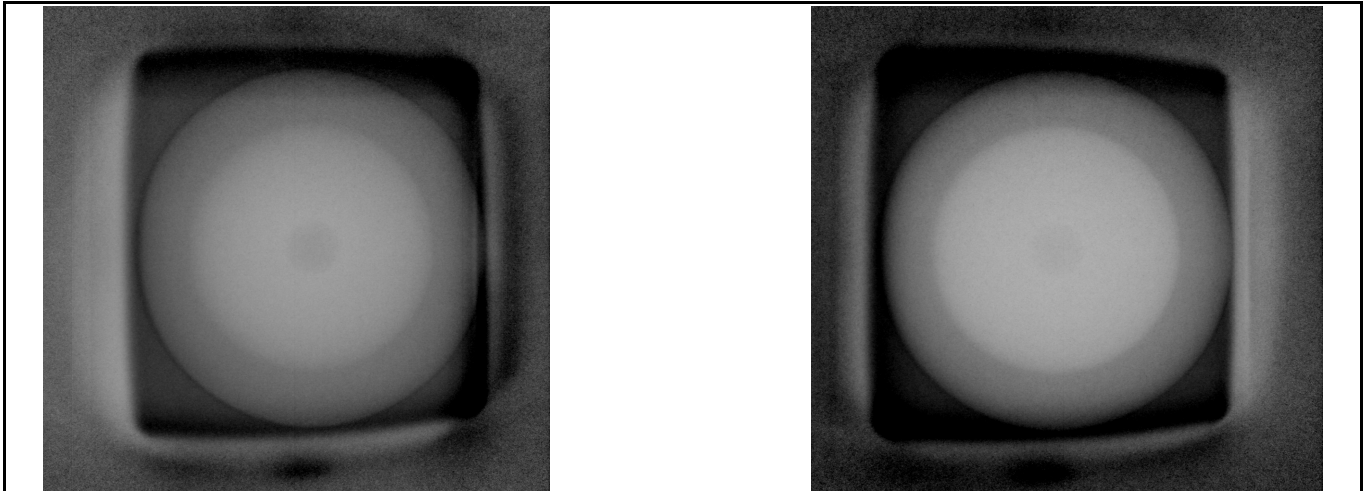


Fig. 8 Results from proton radiograph image plate pictures of the FTO. Shown are “negatives” of the beam distribution normalized images. The left (right) image corresponds to the ~9 (~4.5) mrad collimator. The slightly trapezoidal shaped region is the field of view of the magnetic lens. The outer edge of the copper shell nearly fills the field of view.

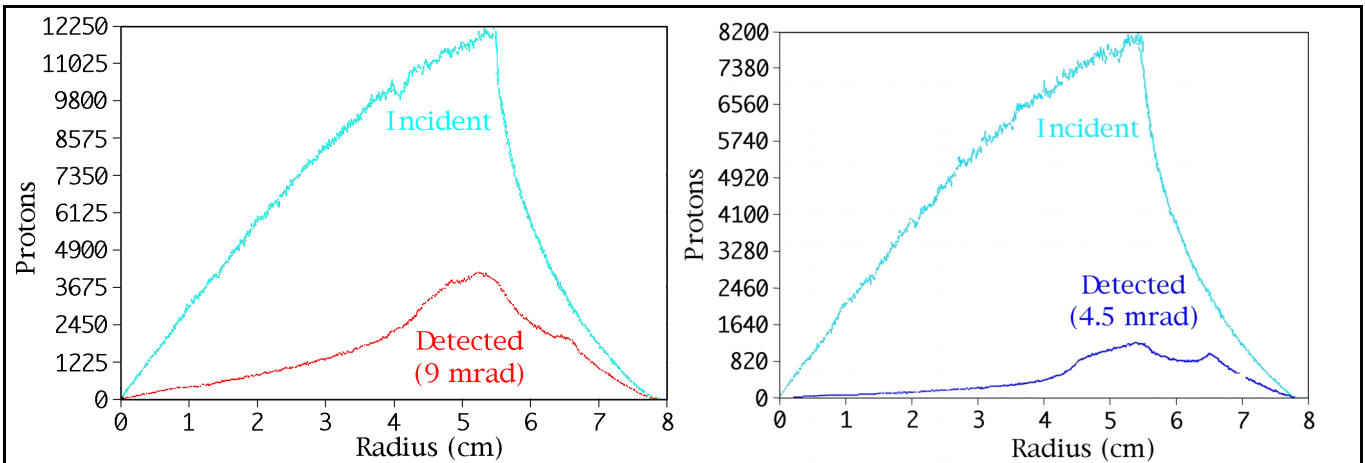


Fig. 9. Radial distributions for the radiographs of FTO similar to those given in Fig. 8, but using the wire chamber data. The left (right) plot is for the 9 (4.5) mrad collimator. The upper (lower) curve is the number of incident (transmitted) particles. The drop to zero in the radial distributions as zero radius is approached is simply a solid angle effect.

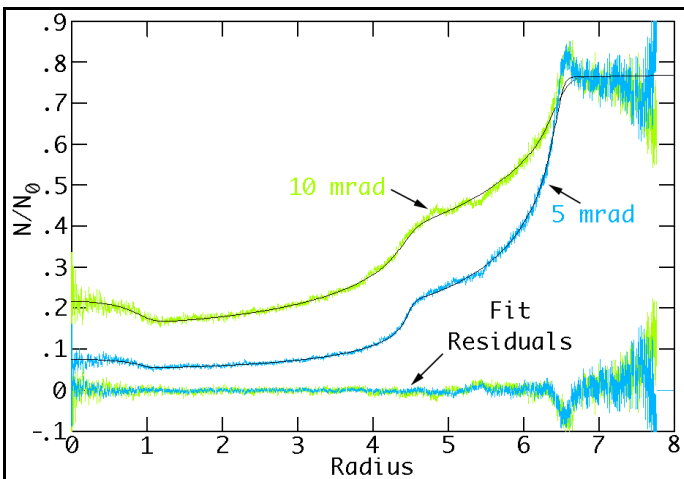


Fig. 10. Fits to the transmission data for the FTO. The upper two curves are the measured transmission vs. radius. The bottom overlaid curves are the residuals of the two fits.

| Material | Radius (cm) | λ (cm) | X_0 (cm) | |
|----------------|-------------|----------------|------------|------|
| Void | 0.98 | – | – | Fit |
| | 1.00 | 0.0 | 0.00 | Real |
| Tungsten alloy | 4.48 | 10.5 | 0.38 | Fit |
| | 4.50 | 10.1 | 0.37 | Real |
| Copper | 6.47 | 14.2 | 1.10 | Fit |
| | 6.50 | 15.1 | 1.42 | Real |
| Foam | – | – | – | Fit |
| | 22.50 | 160.0 | 84.00 | Real |

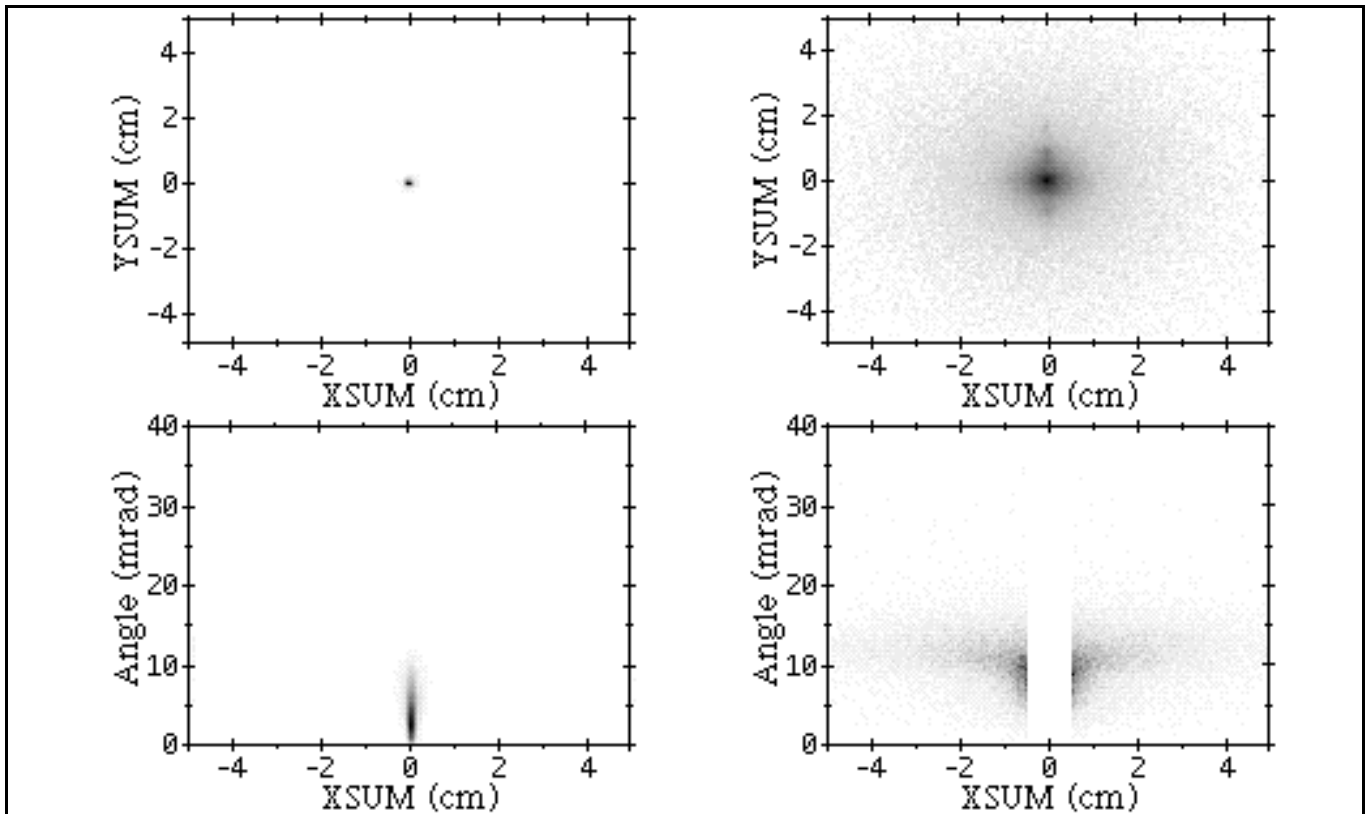
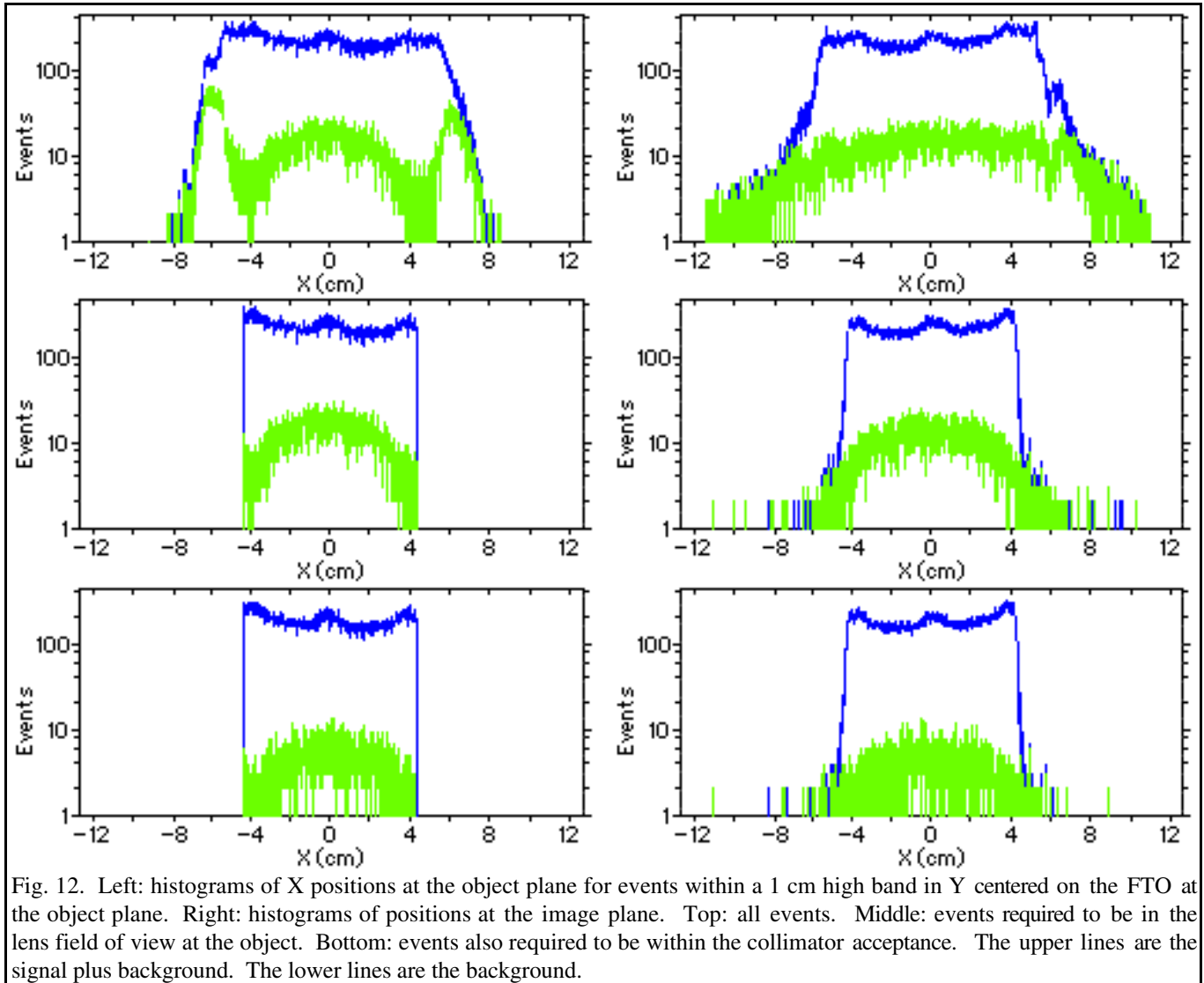


Fig. 11. Top left: two-dimensional histogram of XSUM vs. YSUM on a linear scale; top right on a logarithmic scale; bottom left: XSUM vs. scattering angle on a linear scale; bottom right: on a logarithmic scale with the additional restriction that both $|XSUM|$ and $|YSUM|$ be larger than 5 mm.

majority of events are not “problem” events. The upper right plot is the same data, but plotted on a logarithmic intensity scale to highlight the “problem” events. The bottom left plot shows on a linear intensity scale the proton scattering angle in the object as a function of XSUM and demonstrates that the lens also performs well over the relevant range of scattering angles. The bottom right plot shows the same distribution but on a logarithmic intensity scale and only for “problem” events. The “problem” or background events are defined as those that have both $|XSUM| > 5$ mm and $|YSUM| > 5$ mm. (This explains the missing events in the $|XSUM| \leq 5$ mm region of the plot.) The information on background is more qualitatively given in the histograms shown in Fig. 12. The events shown are from a radiograph of the FTO, where only those events that at the object plane were within a horizontal band of ± 5 mm height centered on the FTO were used. It should be noted that the events considered passed all the way through to the imaging lens and to a trigger counter located behind the wire chambers at the image plane. (This explains the shape of the object plane distributions in Fig. 12, where the central air cavity and copper to tungsten transitions are evident.) The left column gives the X-distribution of those particles measured at the object plane, whereas the right column is for the same particles, but measured at the image plane. Each plot has two curves. The upper curve (darker) curve is for all events, whereas the lower (lighter) curve is for the background events as defined previously. There were several problems with the experimental setup which caused larger than expected backgrounds. One problem was inadequate shielding upstream of the object which allowed particles outside the “field of view” of the upstream lens to reach the object and image plane. Another problem was that the incident beam was by mistake not centered on the object; the majority of the beam actually missing the object and hitting the upstream magnets. The third problem was inadequate thickness for the collimator, which allowed some of the protons that hit the collimator to still reach the image plane. With the use of the wire chamber data, these types of events could be removed. This is shown in the lower two rows of histograms in Fig. 12. The measured “expected” background to signal values can be read off of the bottom row histograms and are on the order of a few percent. A more careful set-up would no doubt have improved these values.



AHF PROTON ACCELERATOR COMPLEX

The AHF will be required to produce transmission radiographic images with high spatial and temporal resolution. From 4 to 16 simultaneously-illuminated views and 25 or more time-separated exposures per view are desired. The desired beam-pulse structure needs to be flexible, with 10^{10} to 10^{11} protons in a 10-20 nsec-long pulse per view. A programmable time separation between pulses in each view which varies from a minimum of about 100 nsec to a maximum of many microseconds. These requirements lead to the use of a low-duty-factor, slowly cycling proton synchrotron with a flexible multipulse beam-extraction system, feeding into a multistage beam-splitting transport system that transmits proton pulses to the test facility.

The total number of protons in the ring is approximately 10^{13} . This number follows from the following arguments. If we want pixel by pixel measurements that have an accuracy of 1 part in A , we need A^2 particles per pixels from counting statistics arguments alone. Allowing for other measurement errors such as those associated with the detectors, we need to boost the number of particles by a factor of B . The beam is attenuated by the object by a factor of C , thus we need A^2BC particles per pixel in the incident beam. Taking into account the area of the object we need an additional factor D given by $(\text{area of object}) / (\text{area of a pixel})$. If we now have E views, assume losses in the beam splitting chain are a factor of F overall, and record G frames per view, the machine must deliver $A^2BCDEFG$ protons in a shot. Going back to Table 1, and taking round number values, we have $A \sim 100$, $B \sim 2$, $C \sim 5$ (the Gaussian shaped

| | |
|-------------------------|-----|
| Total splitter sections | 4 |
| Total straight cells | 120 |
| Total bend cells | 232 |
| Quadrupole Length (m) | 704 |
| bore radius (cm) | 0.5 |
| gradient (T/m) | 2.5 |
| Number of Dipoles | 928 |
| Dipole Length (m) | 2.0 |
| gap (cm) | 5.0 |
| field (T) | 4.2 |

beam centered on the thickest part of the object helps here), $D \sim (10 \text{ cm}/250 \mu\text{m})^2 = 160,000$, $E \sim 16$ (beam splitting in our design is in multiples of 2), $F \sim 2$, and $G \sim 25$, which approximately yields the 10^{13} value.

The nominal beam energy of 50 GeV is set by object thickness and also by the thickness of the vessel (windows) that must contain the blast. The present study is based on an 800-MeV linac, such as available at LANSCE, which injects an H^- beam directly into a 50 GeV synchrotron. Numerous proton synchrotrons in the energy and/or intensity range needed for PRAD are presently in operation around the world. Thus the technology required for a PRAD accelerator has already been demonstrated. A conceptual point design for a system that can meet the above requirements has been presented elsewhere⁸. The synchrotron is fairly conventional, except for use of a lattice with an imaginary transition γ and certain features of the achromatic arcs.

There are two design parameters of a PRAD synchrotron that need some particular attention. First, simplicity of operation and low intensity suggests that a booster stage can be avoided. However, a critical parameter is the magnetic field at injection time. For a 50 GeV synchrotron operating at 1.7 Tesla at full energy, the magnetic field at injection time with 800 MeV injection is 0.05 Tesla. This is thought to be about the minimum practical field. Thus 50 GeV is the maximum practical energy for injection by the existing LANSCE linac at Los Alamos. For a higher energy PRAD synchrotron, either a booster synchrotron, or a higher energy injection linac would be required. (If constructed on a greenfield site, a lower energy linac plus a small booster would be a more cost-effective injector solution.)

The second issue concerns beam extraction from the high-energy synchrotron. If single-turn extraction is chosen, then a pulse train of length equal to the circumference of the synchrotron is delivered to the experiment. For a 1.5 km typical circumference of a 50 GeV synchrotron, this amounts to a total pulse train length of 5 microseconds. The bunch frequency in this train is the rf frequency of the synchrotron. We presently favor a 5 MHz rf frequency, thus providing bunch spacing of 200 ns. Loss-less extraction is possible if the kicker rise time is less than 200 ns, which is obtainable with today's technology.

If single-bunch extraction were to be installed, it would be possible to make a quite flexible program of pulse delivery that extends from spacing of 200 ns up to seconds. The total number of pulses available in the reference scheme would be 25 pulses. For this mode of operation, it is likely that a well-terminated single step kicker of 50 Ohm characteristic impedance would be used. For variable proton burst spacing, a modulator capable of providing 25 pulses with variable pulse spacing would have to be developed. Although no such modulator presently exists, it is believed that its development is not likely to present any obstacles to construction of the facility.

Both beam transport and beam splitting are performed in the beam transport system (see Fig. 13). The beamlines are achromatic and isochronous; the latter feature is enforced by symmetry. In the present example, there are 12 beamlines illuminating the target from different angles, both in-plane and out-of-plane. At the end of each beamline, there is a 45-m target-illuminating section that includes a diffuser and magnetic quadrupoles that prepare the beam size and convergence angles for object illumination. On the opposite side of the object containment chamber from each illuminating section, there are magnetic imaging

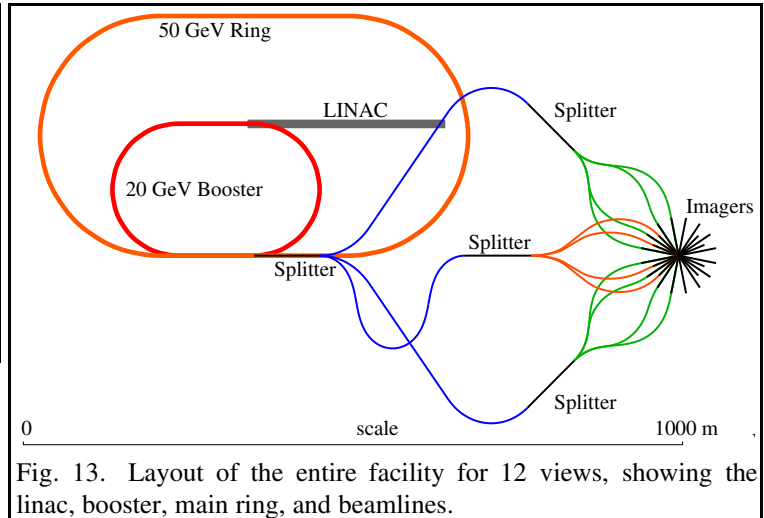


Fig. 13. Layout of the entire facility for 12 views, showing the linac, booster, main ring, and beamlines.

systems and detector arrays. The transport system parameters for the above design are listed in the Table 6 exclusive of the matching and imaging lenses.

CONCLUSION

We have reviewed the basic concept of proton radiography and found that it should perform extremely well and have substantial advantages of x-ray based radiography in the case of thick (100's g/cm^2) objects. In the case of thin objects, it still performs very well, with added bonus that it can be tuned to give high contrast images regardless of how thin the object is. An added feature of proton radiography is the ability to measure, not only the amount of material (as in standard radiography), but also the composition of the radiographed object in terms of material identities. These predictions have been confirmed in beam tests. The proton accelerator needed for a future Advanced Hydrotest Facility is not beyond the scope of existing proton accelerators. Furthermore proton accelerators naturally have the strobed pulse nature needed to follow rapidly evolving dynamic events and can do so for an extended period of time.

¹ InterScience, Inc., "Technology Review of Advanced Hydrodynamic Radiography", March 6-7, 1996, ISI-TM96050701.93.

² H.-J. Ziock et al., "Detector Development for Dynamic Proton Radiography", these proceedings.

³ J. Miyahara et al., "A New Type Of X-Ray Area Detector Utilizing Laser Stimulated Luminescence", Nucl. Instr. and Meth., **A246** (1986) 572.

⁴ Particle Data Group, "Review of Particle Physics", Phys. Rev. **D54**, (1996).

⁵ C.T. Mottershead and J. D. Zumbro, "Magnetic Optics for Proton Radiography", Proceedings of the 1997 Particle Accelerator Conference, Vancouver, B. C., Canada (to be published).

⁶ R. E. Prael, H. Lichtenstein, et. al., "User Guide to LCS: The LAHET Code System", LA-UR-3014, (1989). For more information see <http://www-xdiv.lanl.gov/XCI/PROJECTS/LCS/> or contact R. Prael (505)667-7283.

⁷ A. Fasso, A. Ferrari, J. Ranft, P.R. Sala, G. R. Stevenson, J.M. Zazula, "A Comparison of FLUKA Simulations with Measurements of Fluence and Dose in Calorimeter Structures", Nucl. Instr. and Meth. , **A332** (1993) 459.

⁸ F. A. Neri, H. A. Thiessen, and P. L. Walstrom, "Synchrotrons and Beamlines for Proton Radiography", Proceedings of the 1997 Particle Accelerator Conference, Vancouver, B. C., Canada (to be published).